Pressure-dependent excitonic instability and structural phase transition in Ta_2NiS_5: Raman and first-principles study

Sukanya Pal,[1,2,*,†] Arijit Sinha,[3,*] Luminita Harnagea,[4] Prachi Telang,[5] D. V. S. Muthu,[1] U. V. Waghmare,[3] and A. K. Sood[1]

[1]*Department of Physics, Indian Institute of Science, Bangalore 560012, India*
[2]*Department of Physics and Astronomy, George Mason University, Virginia 22030, USA*
[3]*Theoretical Sciences Unit, Jawaharlal Nehru Centre for Advanced Scientific Research, Bangalore 560064, India*
[4]*I-HUB Quantum Technology Foundation, Indian Institute of Science Education and Research, Pune, Maharashtra-411008, India*
[5]*Department of Physics, Indian Institute of Science Education and Research, Pune, Maharashtra-411008, India*

(Received 17 September 2023; revised 28 February 2024; accepted 26 March 2024; published 22 April 2024)

Ta_2NiS_5, a semiconductor at ambient conditions, does not exhibit an excitonic insulating state like its selenium counterpart Ta_2NiSe_5, owing to its large band gap. Using a combination of Raman spectroscopy and analysis with first-principles effective Hamiltonian, we explore its instability toward an excitonic insulating state as a function of pressure, and affirm that excitonic insulating state does not get stabilized in Ta_2NiS_5 with pressure. We observe pressure-induced structural phase transition from its orthorhombic *Cmcm* structure to another orthorhombic *Pmnm* structure, with onset at $\sim$ 4.2 GPa and this transition gets completed at $\sim$ 6 GPa. We observe Raman signatures of an additional phase transition at $\sim$ 10.8 GPa, which is suggested to be associated with a semiconductor to metal transition.

DOI: 10.1103/PhysRevB.109.155202

I. INTRODUCTION

An excitonic insulator (EI) is an exotic phase of matter manifested in the strong electron-hole coupling limit in a small bandgap semiconductor or semimetallic systems. Knox [1] showed that in a conventional insulator, when the binding energy of an exciton $|E_B|$ exceeds the energy gap E_g, the insulating ground state would be unstable against the formation of excitons and excitonic condensation with a macroscopic phase coherence taking place below a certain critical temperature T_c. In solids with small band-gap, there may thus exist a phase at sufficiently low temperature called the excitonic insulator [2,3]. $TiSe_2$ [4,5], $TmSe_{0.45}Te_{0.55}$ [6–8] and Ta_2NiSe_5 [9–12] are a few examples of EI. Ta_2NiSe_5 (TNSe) is an EI which is located in the semiconducting side of the EI phase diagram [9]. Ta_2NiS_5 (TNS) a material with selenium replaced with sulfur, is a semiconductor which has been reported not to possess any excitonic insulating state at ambient conditions. This motivated us to explore pressure-induced structural and excitonic instabilities in Ta_2NiS_5.

Ta_2NiS_5 and Ta_2NiSe_5 are layered compounds which crystallize in the orthorhombic and monoclinic space groups, respectively. Even though the constitutional units of the two compounds are similar, their symmetry operations are different, resulting in them having different space groups. There exists a twofold screw axis along the *c* axis in the structure of Ta_2NiS_5, but not in Ta_2NiSe_5 [13]. Ta_2NiS_5 has a larger electronic bandgap than Ta_2NiSe_5 because of the fact that increased isovalent substitution of Se with S, the hybridization between Ni 3*d* and Se 4*p* (S 3*p*) orbitals is weakened. This results in lowering of the energy states at the top of the valence band while the conduction band is almost unaffected and an overall enhancement of the band gap E_g occurs, compared to Ta_2NiSe_5. With increasing S substitution, changes in the Ta-chalcogen hybridization enhance the band gap by affecting the energetically higher lying Ta-*d* bands above 1 eV [14]. The exciton binding energy relative to bandgap is thus smaller resulting in suppressed excitonic instability. Ta_2NiS_5 does not exhibit the same excitonic signatures such as band flattening and band gap opening below a critical temperature like Ta_2NiSe_5. However, a structural transition has been reported at 120 K [15] without forming any flat bands or, a metal to semiconductor transition. Ta_2NiS_5 has a thickness independent robust band gap of $\sim$ 0.2 eV [16]. Resistivity measurements of Ta_2NiS_5 showed no sign of phase transition until $T \sim 680$ K and that its resistivity is larger than that of Ta_2NiSe_5 [17]. Magnetic susceptibility measurements reveal the diamagnetic nature similar to that of TNSe, but no sharp changes above 300 K. However, a reversible jump occurs at 28 K, which indicates a first-order phase transition. The resistivity becomes too large to be measured at this temperature indicating an insulating behavior [17]. Ellipsometry experiments [14] show that the exciton-phonon complexes are sparse in Ta_2NiS_5 and do not develop a long-range order. The spectral weight of excitonic resonances observed in Ta_2NiS_5 is less compared to Ta_2NiSe_5 and strong Fano interference with the continuum excitations indicate that exciton dressing with the cloud of phonons localizes the exciton states [14]. A recent time-resolved angle-resolved photoemission spectroscopy study shows that band gap of Ta_2NiS_5 collapses by

*These authors contributed equally to this work.
†spal5@gmu.edu

optical excitation, similar to Ta_2NiSe_5 [18]. Thus, the electronic structure might have interesting properties even though Ta_2NiS_5 does not show any phase transition. It would be interesting to study the pressure-dependent evolution of electronic structure of Ta_2NiS_5 and its comparison with Ta_2NiSe_5.

Our aim in this paper is to investigate the effect of pressure on structural and electronic properties of Ta_2NiS_5 and explore pressure-induced excitonic instability of Ta_2NiS_5 and compare this analysis with previously reported pressure-induced transitions observed in the EI compound Ta_2NiSe_5. Here, we use a combination of Raman experiments, first-principles density functional theory (DFT) and Bardeen-Cooper-Schrieffer -like model Hamiltonian analysis to confirm that excitonic insulating phase cannot be stabilized in Ta_2NiS_5 with pressure. Both our experimental and theoretical results indicate an onset of structural phase transition at $P \sim 4.2$ GPa. The structural transition gets completed at $P \sim 6$ GPa resulting in change in the ambient orthorhombic *Cmcm* structure to another orthorhombic *Pmnm* structure. Our Raman experiments suggest another phase transition at $P \sim 10.8$ GPa which we associated with an insulator to metal transition with evidence from calculations.

II. EXPERIMENTAL DETAILS

Using iodine as a transporting agent, the chemical vapor transport method was employed to grow Ta_2NiS_5 single crystals with growth parameters as described in Refs. [19,20] for the growth of Ta_2NiSe_5 single crystals. Fine powder of polycrystalline Ta_2NiS_5 and a few mg of iodine, were loaded in a quartz ampoule and sealed under vacuum. The ampoule was placed in a three-zone tube furnace, where a gradient of 50 °C (870 °C/820 °C) was maintained between the source and sink zones. After over a week of transport, many needle -shaped single crystals were obtained.

We used x-ray diffraction [Bruker D8 diffractometer (Cu Kα) and Bruker, KAPPA APEX II CCD DUO, Mo Kα), Laue diffraction (Photonic Science UK)], and a scanning electron microscope (ZEISS Ultra Plus) equipped with an energy dispersive x-ray spectroscopy probe (EDX) to verify the phase purity, crystal quality, and orientation, crystal structure parameters, homogeneity, and chemical composition. The single crystals are single phase, crystallizing in an orthorhombic phase, space group *Cmcm* (No. 63), with lattice parameters $a = 3.4124$ Å, $b = 12.1473$ Åand $c = 15.1121$ Å, in good agreement with the high-quality structural data reported by Sunshine *et al.* [13]. The x-ray diffraction measurements indicate that the single crystals are of good quality, with the *b*-axis perpendicular to the layers (*ac* plane) and growing predominately along the *a* axis. The chemical composition and homogeneity were verified by recording EDX data on several pieces of single crystal and the samples were observed in backscattered-electron modeWithin the error bar of the technique (1 at. %) the samples are stoichiometric and homogeneous.

Electrical resistivity and specific heat measurements were performed using a Physical Property Measurement System (PPMS/Quantum Design, USA). The resistivity was measured as a function of temperature in the interval 30 to 380 K. It shows an insulating behavior and does not exhibit any phase transition, as previously reported [9,15]. The specific heat was measured using the relaxation method and no phase transition was captured down to 2 K. High-pressure Raman studies were performed up to 19.1 GPa at room temperature using a Mao-Bell type diamond anvil cell (DAC). A very small piece from the bulk crystal ($\sim$ 30 μm), along with a very small ruby chip ($\sim$ 10 μm) were placed inside a hole of diameter $\sim$ 200 μm in a stainless steel gasket kept between the two diamonds of the DAC. A methanol-ethanol (4:1 ratio) mixture was used as a pressure transmitting medium. A ruby fluorescence method [21] was used for pressure calibration. Raman spectra were recorded in LabRam spectrometer (M/s Horiba) in backscattering geometry, using 50X objective and laser excitation of 532 nm from a diode-pumped solid state laser.

III. COMPUTATIONAL DETAILS

Our first-principles calculations are based on DFT as implemented in the QUANTUM ESPRESSO package [22]. Interactions between valence electrons and ionic cores are modeled using projector-augmented-wave potentials generated by Dal Corso [23]. We used Perdew-Bruke-Ernzerhof functional of exchange-correlation energy of electrons with a generalized-gradient approximation [24]. Energy cutoffs of 45 and 320 Ry were used to truncate plane wave basis-sets used to represent Kohn-Sham (KS) wave functions and charge density, respectively. Brillouin zone (BZ) integrations were sampled on a uniform mesh of $8\times8\times3$ and $10\times6\times2$ **k** points in calculations of *Cmcm* and *Pmnm* phases, respectively with a Fermi-Dirac smearing width of $k_BT = 0.003$ Ry. For accurate description of the van der Waals (vdW) interaction between the layers nonlocal optB88-vdW [25–30] exchange-correlation energy functional was used in all the calculations. Self-consistent numerical solution of the KS equation was obtained with convergence of total energy within 10^{-8} Ry. Structures were relaxed by minimizing total energy, until Hellman-Feynman forces on each atom converge within 10^{-4} Ry/Bohr using Broyden-Fletcher-Goldfarb-Shanno method.

Since DFT typically overestimates electronic bandwidth of *d*-orbital bands, and Ta, Ni have partially filled *d* orbitals, we used an on-site Hubbard-*U* parameter [31,32], $U = 6.0$ eV at Ta-5*d* orbitals [19] to capture the correct electronic bandgap. We find properties (electronic bandgap, lattice parameters) of TNS are insensitive to *U* at Ni-3*d* orbitals (for more details see Tables S I and II and Fig. S7 of Supplemental material [33]), hence did not incorporate it in the calculations. We obtained dynamical matrix and phonon spectrum at Γ-point using frozen phonon method implemented in PHONOPY code [35], and have used the SPGLIB library [36] to determine symmetry of the structures.

IV. RESULTS AND DISCUSSIONS

A. Experimental section

Ta_2NiS_5 crystallizes in orthorhombic *Cmcm* space group and the unit cell consists of 32 atoms and 16 atoms in the primitive unit cell, giving 48 vibrational modes at the Γ point of the BZ. The irreducible representation of the optical phonons at the Γ point include Raman modes of A_g

and B_{2g} symmetries. We observe 11 Raman modes inside the DAC at starting pressure of 0.2 GPa (see bottom panels of Fig. 1) marked as: M1 (40.1 cm^{-1}), M2 (46.7 cm^{-1}), M3 (64.1 cm^{-1}), M4 (127.7 cm^{-1}), M5 (150.1 cm^{-1}), M6 (271.8 cm^{-1}), M7 (294.5 cm^{-1}), M8 (321.5 cm^{-1}), M9(345.6 cm^{-1}), M10 (389.2 cm^{-1}), and a very weak mode M11 (418.5 cm^{-1}). Figure 1 shows the Raman spectra of Ta_2NiS_5 at a few pressures and each spectrum is demonstrated in four spectral regions for better visualization of Raman modes. Noticeable changes are observed in the Raman modes appearing in the spectral range of 115–380 cm^{-1} as seen in Figs. 1(b) and 1(c). The following features are noteworthy: Raman spectrum recorded at ∼ 4.6 GPa depicts that Raman modes M8 and M9 [marked by asterisk at the bottom panel of Fig. 1(c)] and mode M11 [marked by asterisk at the bottom panel of Fig. 1(d)] are absent. Five new Raman modes M12, M13, M14, M16, and M17 (marked by arrows) appear at ∼ 4.6 GPa. Raman modes M4 and M5 [marked by asterisk in Fig. 1(b)] are absent in the Raman spectrum observed at ∼ 6.2 GPa, while a new mode M15 [marked by arrow in Fig. 1(c)) appears. Raman mode M16 (marked by asterisk in Fig. 1(c)] is absent in the Raman spectra recorded at ∼ 12.1 GPa. The top panel of Fig. 1 shows the Raman spectrum at ∼ 0.1 GPa in the return pressure cycle, indicated by (R) next to the pressure value, which shows that the pressure effects are reversible.

Pressure dependence of the mode frequencies as extracted from Lorentzian fits to the spectra, [see Fig. 2(a)] is fitted (solid lines) to $\omega_P = \omega_0 + (d\omega/dP)P$. The following observations can be made from Fig. 2(a): (i) At ∼ 4.2 GPa, modes M8, M9 and M11 disappear and new modes M12, M13, M14, M16, and M17 appear. The integrated intensities of modes M8 and M9 decrease to zero at ∼ 3.3 GPa (as shown in Fig. S1 of the Supplemental Material [33]) and combined with the fact that the modes M8 and M9 are absent at the spectrum recorded at an intermediate pressure value of 3.7 GPa (as shown in Fig. S2 of the Supplemental Material [33]) suggest that Raman modes M16 and M17 are new modes that appear at ∼ 4.2 GPa and they are not the continuation of Raman modes M8 and M9, respectively. The pressure coefficients $d\omega/dP$, of the Raman modes M1, M2, M3, M6, and M10 change at this pressure value. (ii) Modes M4, M5 disappear while a new mode marked M15 appear at ∼ 6.0 GPa. (iii) At ∼ 10.8 GPa, mode M16 disappears and the pressure coefficients of modes M1, M2, M14 change. The first observation, marks the onset of a phase transition at $P_1 \sim 4.2$ GPa, which can be associated with structural changes from orthorhombic *Cmcm* phase (ambient) to another orthorhombic *Pmnm* (HP1 structure) (to be discussed later). The phase transition gets completed at ∼6 GPa. The signature of another phase transition is observed at $P_2 \sim 10.8$ GPa, which can be associated with changes in electronic structure (to be discussed later). The signature of these two transitions is also evident from the variation of linewidths of Raman modes as a function of pressure (as shown in Fig. S 3 of the Supplemental Material [33]).

B. Theoretical calculations

1. Relaxed crystal and electronic structure at P = 0 GPa

At ambient conditions, TNS exists in orthorhombic *Cmcm* phase [17] with four formula-units (f.u.) in the conventional unit cell [see Fig. 3(a)]. We use primitive-cell [16 atoms, 2 f.u. see Fig. 3(b)] in our calculations. Dependence of theoretical estimates of lattice parameters on vdW interaction within Grimme-D2 scheme, optB88-vdW functional and Hubbard-U parameter at Ta-5d orbitals given in Tables SI and II of the Supplemental Material [33], show that the lattice parameter a (Ni-Ta-Ni chain direction) is sensitive to Hubbard-U parameter, whereas b (layer direction) and c parameters are affected by the flavor of vdW correction. We find that optB88-vdW functional and Hubbard-U = 6.0 eV at Ta-5d orbitals describe the structure of Ta_2NiS_5 well in terms of lattice parameters and electronic structure (see Sec. I, Table SI and II, and Fig. S6 of the Supplemental Material [33] for details). Our estimates of lattice parameters are $a = 3.45$ Å, $b = 12.13$ Å, $c = 14.99$ Å which are in good agreement with our experimental data ($a = 3.4124$ Å, $b = 12.1473$ Å, $c = 15.1121$ Å), as well as the lattice parameters reported by Sunshine *et al.* [13] ($a = 3.415$ Å, $b = 12.146$ Å, $c = 15.097$ Å) see Table I for relaxed atomic positions of Ta_2NiS_5 at $P = 0$ GPa *Cmcm* structure.

TABLE I. Atomic positions in the relaxed *Cmcm* structure of TNS at $P = 0$ GPa, obtained using optB88-vdW functional and $U = 6.0$ eV at Ta-5d orbitals, and comparison of those with experimentally obtained one.

		Theory			Experiment [13]		
Atom	Site	x	y	z	x	y	z
Ta	8f	0.0	0.2206	0.1084	0.0	0.22082	0.10879
Ni	4c	0.0	0.7001	0.25	0.0	0.69292	0.25
S(1)	8f	0.5	0.0839	0.1353	0.5	0.08282	0.13527
S(2)	8f	0.0	0.1490	0.9498	0.0	0.14850	0.94974
S(3)	4c	0.0	0.3202	0.25	0.0	0.31968	0.25

At $P = 0$ GPa, the orthorhombic *Cmcm* phase of Ta_2NiS_5 is a semiconductor with a band gap ∼ 0.26 eV [9,37] at Γ point. Our calculation with optB88-vdW functional and Hubbard-U = 6.0 eV at Ta-5d orbitals [19] give an electronic structure with a band gap of 0.39 eV at the Γ point [see Fig. 3(d)], which compares well with the experiment. Orbital projected density of states show that the states at conduction band minimum (CBM) are dominated by Ta-5d orbitals and those at valence band maximum (VBM) are constituted mainly of Ni-3d and S-3p orbitals. We have not used on-site electronic correlations (Hubbard-U parameter) at Ni-3d orbitals, which neither change electronic bandgap nor substantially change the lattice parameters of TNS in *Cmcm* crystal structure (see Tables I, II, and Fig. S 7 of the Supplemental Material for details [33]).

2. Zone center phonons and dynamic stability (P = 0 GPa)

We determined phonon eigenmodes and frequencies of *Cmcm* crystal structure of Ta_2NiS_5 at $P = 0$ GPa at Γ point of the Brillouin zone using the frozen-phonon method, and studied their dependence on Hubbard-U parameter at Ta-5d orbitals. We note significant change in frequencies of certain phonon modes, see Figs. 4(b)–4(d) for visualization of those modes and their symmetry irreducible representations, which reveals these modes predominately involve displacement of

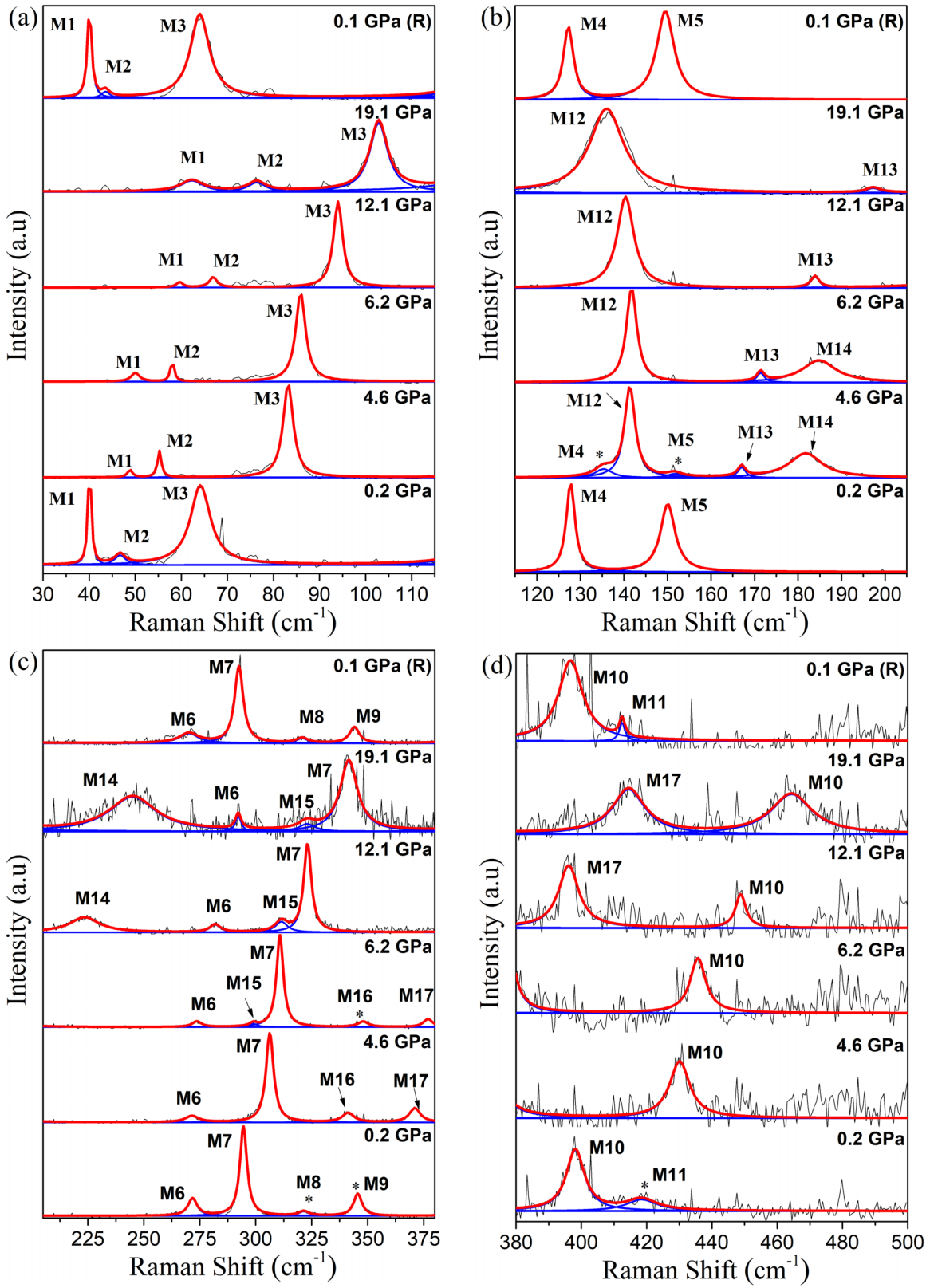

FIG. 1. Pressure evolution of Raman spectra in the spectral range of (a) 30–115 cm^{-1}, (b) 115–205 cm^{-1}, (c) 205–380 cm^{-1}, and (d) 380–500 cm^{-1} respectively. Solid lines (red and blue) are the Lorentzian fits to experimental data points (black). Disappearance/appearance of new modes is indicated by asterisk symbol and arrows respectively. The top panel shows the Raman spectrum at $\sim$ 0.1 GPa in the return pressure cycle, indicated by R next to the pressure value.

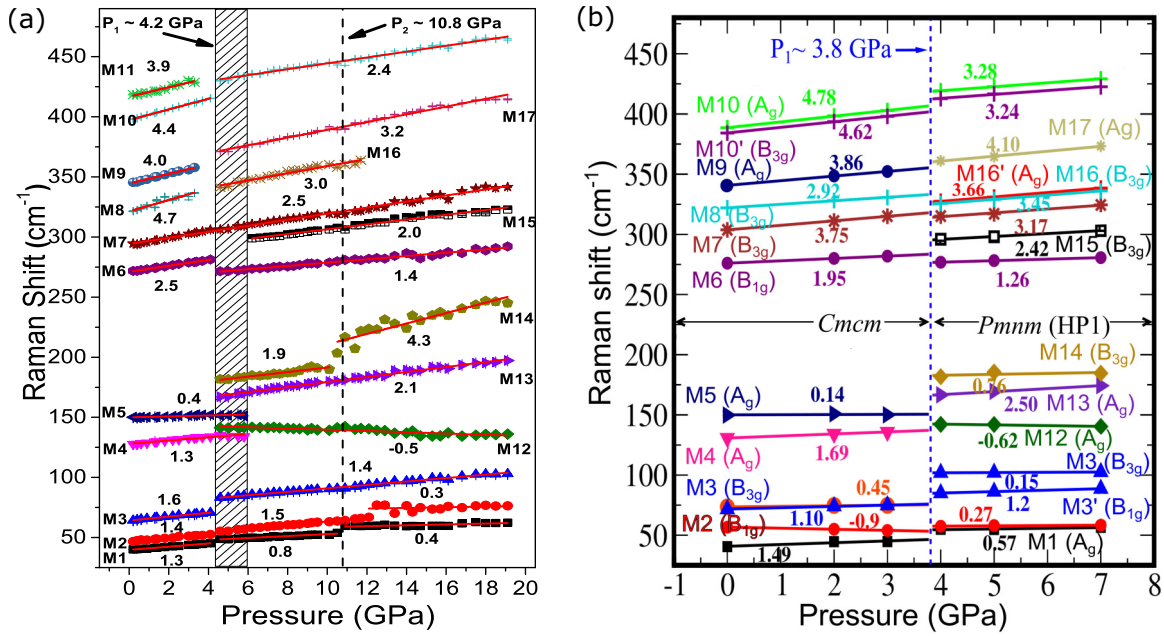

FIG. 2. (a) Raman shift versus pressure plot. Solid red lines are linear fits to the observed frequencies. The numbers next to the straight lines are the fitted value of $d\omega/dP$ in cm^{-1}/GPa. The vertical shaded region from $P \sim 4.2$ to 6.0 GPa denotes the onset and completion of first phase transition and the black dashed line at $P \sim 10.8$ GPa denotes the second phase transition. (b) Calculated frequencies of Raman active phonon modes at Γ point, numbers denote pressure slope of linear fit which is in good agreement with experiments. The blue dashed line denotes the theoretically calculated first transition at $P \sim 3.8$ GPa. Different symbols and colors are used to denote phonon modes having specific symmetry irreducible representations of the respective space groups. Please note, we provide calculated Raman spectra till $P = 7$ GPa, because the high-pressure phase ($P > 10$ GPa) remains unidentified.

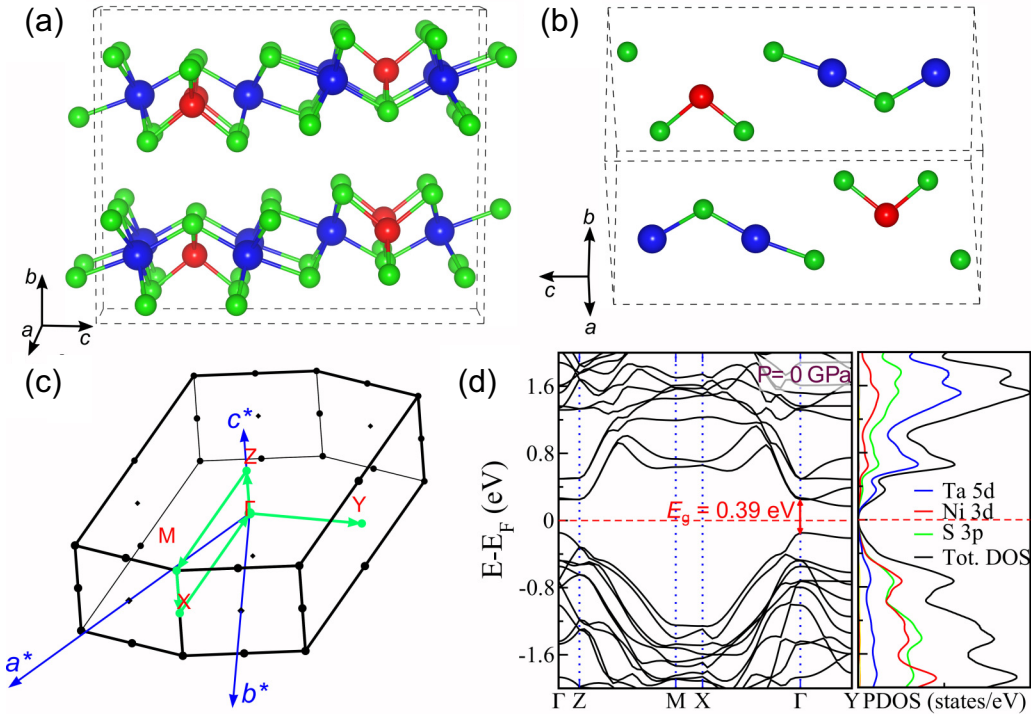

FIG. 3. (a) Conventional and (b) primitive unit cells of Ta_2NiS_5 in *Cmcm* crystal structure, and (c) Brillouin zone of primitive cell with high symmetry path shown in green, (d) electronic structure exhibits a gap of $E_g = 0.39$ eV at the Γ point, and orbital-projected density of states show Ta-5*d* orbitals dominate the states at conduction band minimum (CBM) and Ni-3*d*, S-3*p* orbitals contribute primarily to the states at the valence band maximum (VBM).

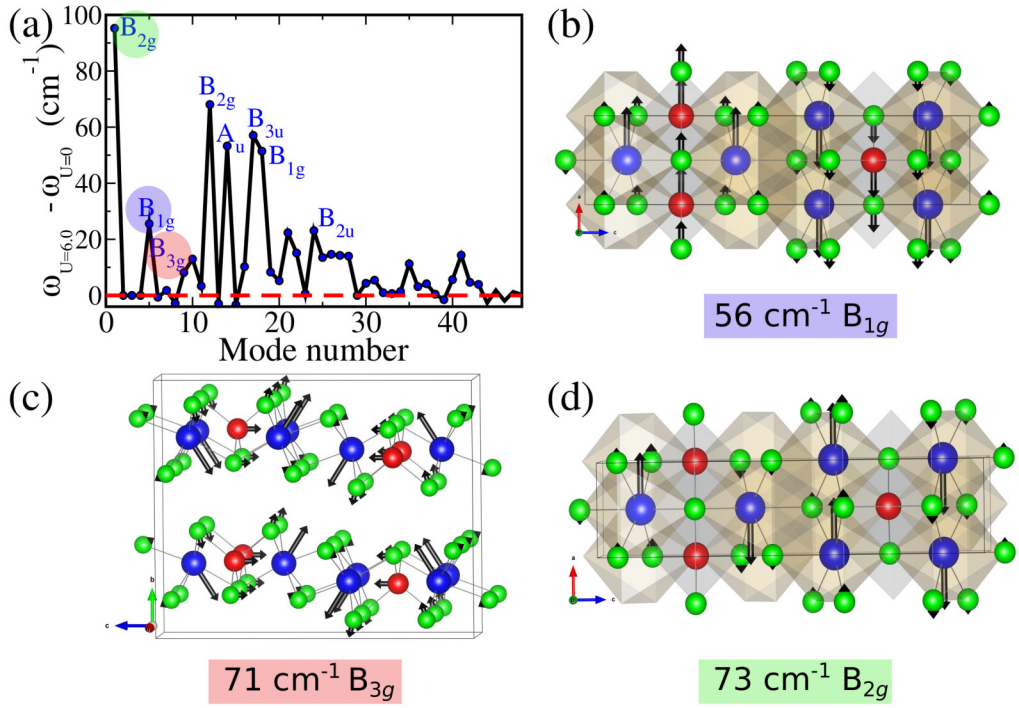

FIG. 4. (a) Difference in zone center frequencies of phonons of orthorhombic (*Cmcm*) Ta_2NiS_5 at $P = 0$ GPa calculated using Hubbard-$U = 0$ eV and 6 eV (at Ta 5*d* orbitals). Symmetry irreducible representations (irreps.) are given for the modes exhibiting frequency changes larger than 20 cm^{-1}. Modes marked with colored circles in (a) are visualized in (b), (c), and (d). Black arrow denotes displacement of ions. Ta, Ni and S are denoted by blue, red and green balls, respectively, and solid black box displays conventional unit cell of the orthorhombic *Cmcm* crystal structure.

Ta atoms. The change in Hubbard-U parameter from 0 to 6 eV (applied at Ta 5*d* orbitals), primarily affects electronic states near the valence band maximum. The dependence of the phonon frequencies on U is related to electron-phonon coupling in Ta_2NiS_5. Lattice parameters of Ta_2NiS_5 (at $P =$ 0 GPa) are also sensitive to Hubbard-U parameter (see Table SIII of the Supplemental Material [33] for details), which indicates coupling of electrons with acoustic phonons.

We find an unstable B_{2g} phonon mode with imaginary frequency of $14i$ cm^{-1} in the orthorhombic (*Cmcm*) Ta_2NiS_5 at $P = 0$ GPa and Hubbard-$U = 0$ eV, which was also reported earlier by Subedi (see Ref. [38]) and, argued as a reason for the existence of low temperature monoclinic $C2/c$ crystal structure which can, host an EI state. However, no such EI state is reported in Ta_2NiS_5 which remains a semiconductor down to low temperatures and all pressures. Inclusion of Hubbard-$U = 6.0$ eV at Ta 5*d* orbitals in phonon calculations removes the B_{2g} lattice instability and makes Ta_2NiS_5 dynamically stable (see Table SIII of Supplemental Material [33]) in the orthorhombic *Cmcm* crystal structure at $P = 0$ GPa, consistent with experiments. This suggests the importance of electronic correlations in Ta_2NiS_5, and a large change in ω of unstable phonon involving mostly Ta displacements from $14i$ cm^{-1} to ~ 70 cm^{-1}, on inclusion of U reveals its strong electron-phonon coupling (see Fig. 4).

3. *Pressure dependent structural transitions*

The crystal structures of high pressure phases of TNS have not been characterized. As a similar structural transition was observed in Ta_2NiSe_5 [11,19], we take a hint from this to simulate structure of Ta_2NiS_5 phase stabilizing above $P = 4$ GPa. We have two candidate crystal structures for this, (*i*) orthorhombic *Pmnm* (HP1) or (*ii*) monoclinic $P2/n$ (HP1')(see Supplemental Material (SM) Tables SIV and V and Fig. S4 [33] for details of the optimized crystal structures and their visualizations). Transitions to both of these phases involve sliding of the alternate layer along *a* (Ta-Ni-Ta chain) direction. Evolution of the enthalpy difference $(H_X - H_{Cmcm})$, where $X = Pmnm$ (HP1) or $P2/n$ (HP1') of these structures (see Sec. II of the SM for details of construction and simulation of HP1 and HP1' structures of TNS) clearly shows [see Fig. 5(a)] that HP1 and HP1' structures stabilize above 3.8 GPa and 3.0 GPa, respectively.

Moreover, our calculated P dependence of enthalpy difference (see supplementary material Fig. S 5 [33]) reveals that structural transition from *Pmnm* to $P2/n$ structure at high pressures ($\sim$10 GPa) is not possible (see Fig. 5). While we fail to predict the second high pressure phase (HP2) around 10 GPa, we show that electronic band gap of Ta_2NiS_5 shrinks with P and it becomes metallic at $P \sim 10$ GPa (see SM Fig. S4 for details), suggesting that the observed transition at $P \sim 10$ GPa is likely to be an insulator to metal transition.

4. *Stability of EI phase in C2/c crystal structure of* Ta_2NiS_5

To probe the stability of EI phase of Ta_2NiS_5 in $C2/c$ crystal structure, we have used a phenomenological

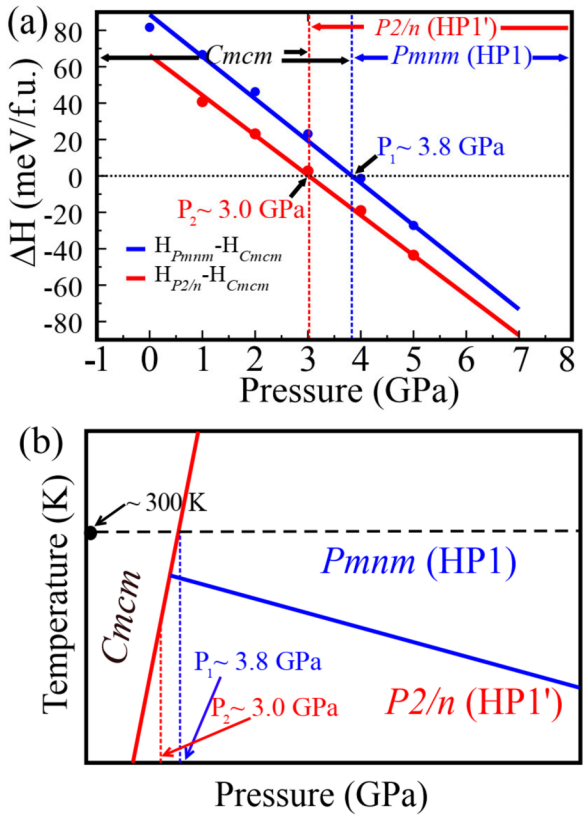

FIG. 5. (a) Evolution of relative enthalpies of *Pmnm* (HP1) and $P2/n$ (HP1') crystal structures of Ta_2NiS_5 with pressure. There is a transition to HP1 structure at $P \sim 3.8$ GPa (observed experimentally at room temperature) and transformation to HP1' structure is around 3.0 GPa (at low temperature). (b) Schematic phase diagram of Ta_2NiS_5 sketched based on our calculations.

model [19]:

$$E = f_c(\epsilon_c - \epsilon_v) + 2\epsilon_v + \sum_\nu \left(\frac{1}{2}K_\nu u_\nu^2 + f_c F_\nu u_\nu\right), \quad (1)$$

where f_c is the population of electrons in the conduction band, and ϵ_c (ϵ_v) is the energy of the conduction (valence) band, K_ν, u_ν are effective spring constant and amplitude of optical phonon mode ν and F_ν is its coupling with an exciton, which involves excitation of an e^- from the valence band $|V\rangle$ to conduction band $|C\rangle$. F_ν is estimated from the projection of Hellman-Feynman force vector (arising from formation of an exciton) onto the eigenmode $|\nu\rangle$ of the force constant matrix:

$$f_c\langle C|\Delta V_\nu|V\rangle + f_v\langle V|\Delta V_\nu|V\rangle + F_0 = \langle F|\nu\rangle, \quad (2)$$

in Eq. (2), $F_0 = \sum_i \langle i|\Delta V_\nu|i\rangle$ is the force due to all electronic states lower in energy than the VBM $|V\rangle$, $\Delta V_\nu = \frac{\partial V_{KS}}{\partial u_\nu}\Delta u_\nu$. The ground state of the model in Eq. (1) is obtained by minimizing E wrt u_ν, which gives renormalized (optimized) energy:

$$E_{\min}\left(u_{\nu,\min} = -\frac{f_c F_\nu}{K_\nu}\right) = f_c(\epsilon_c - \epsilon_v) + 2\epsilon_v - \sum_\nu \frac{F_\nu^2 f_c^2}{2K_\nu}, \quad (3)$$

where $(\epsilon_c - \epsilon_v)$ is the energy required to create an exciton and the second term is the energy gain from renormalization by phonons. For stability of an EI phase, $E_{\min}$ should be negative, which gives the following criteria :

$$E_g < \sum_\nu \frac{F_\nu^2}{2K_\nu}. \quad (4)$$

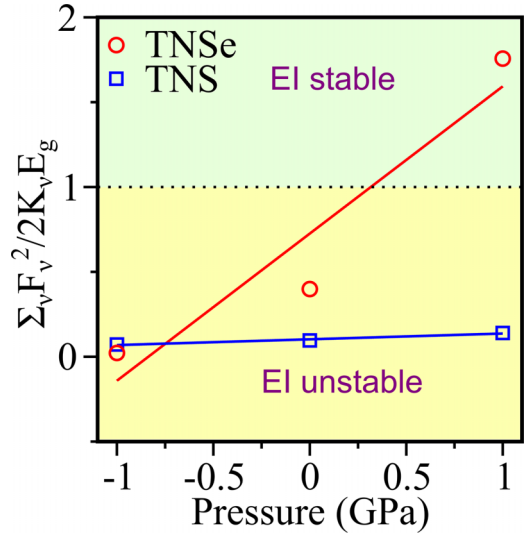

FIG. 6. Variation in the estimated $\sum_\nu \frac{F_\nu^2}{2K_\nu E_g}$ of Ta_2NiS_5 (blue) and Ta_2NiSe_5 (red) in $C2/c$ crystal structure with pressure confirms no onset of excitonic instability of Ta_2NiS_5 at low pressures in contrast to Ta_2NiSe_5 (please note, EI phase is stable in the region above the horizontal dotted line).

In Eq. (4) we set $E_g = \epsilon_c - \epsilon_v$, $f_c = 1$, and $\epsilon_v = 0$. A soft phonon mode $|\nu\rangle$ (small K_ν) coupling strongly with an exciton (large F_ν) should contribute greatly to the EI stability.

To obtain all the parameters of model Hamiltonian given in Eq. (1) from first-principles, we simulate $2\times2\times1$ supercell of optimized structure for Ta_2NiS_5 in $C2/c$ phase with Γ-point sampling. We simulate an excitonic configuration by constraining occupation of electrons in states at the Γ point, and determine force vector $|F\rangle$ (on each atom) and obtain F_ν as the projection: $F_\nu = \vec{F}\cdot\hat{e}_\nu$. We examine the evolution of $\sum_\nu \frac{F_\nu^2}{2K_\nu E_g}$ with hydrostatic pressure (see Fig. 6).

From Fig. 6 it is evident that $\sum_\nu \frac{F_\nu^2}{2K_\nu E_g} < 1$ for Ta_2NiS_5 in $C2/c$ crystal structure, and the excitonic insulator phase does not stabilize at low pressures, it remains semiconducting in contrast to Ta_2NiSe_5 [19].

5. Comparison between theory and experiments

In experiments, we observed that Ta_2NiS_5 at room temperature undergoes structural phase transformations with pressure at $P = 4$ and 10 GPa, evident in the discontinuities in measured frequencies from pressure-dependent Raman spectra [see Fig. 2(a)]. The first transition is at $P = 4$ GPa, which is close to the calculated transition pressure (3.8 GPa) HP1 structure (*Pmnm*). Our estimated Raman active phonon mode discontinuities, considering the transition from the *Cmcm* to the *Pmnm* (HP1) structure, agrees well with experimental Raman results [see Fig. 2(a)]. Hence, we interpret that the first pressure driven transition in Ta_2NiS_5 observed at room

temperature at $P \sim 4$ GPa is a transition from the *Cmcm* to the *Pmnm* (HP1) structure. We also predict that at low T, Ta_2NiS_5 has a possibility to transform from *Cmcm* to $P2/n$ crystal structure (like Ta_2NiSe_5) see the schematic phase diagram of Ta_2NiS_5 in Fig. 5(b). However, we do not have a reference crystal structure of Ta_2NiS_5 for pressures beyond 10 GPa (HP2), because no structural phase transition of Ta_2NiSe_5 is reported for $P \geqslant 10$ GPa. The higher pressure ($P \geqslant 10$ GPa) phase of Ta_2NiS_5 (HP2) remains unidentified in this study.

V. CONCLUSIONS

In conclusion, using a combination of Raman experiments and theoretical analysis with first-principles effective Hamiltonian, we show that Ta_2NiS_5 does not exhibit an instability to excitonic insulating state as a function of pressure. The Raman signature of phase transition at ~ 4 GPa, has been associated with a structural transition, from orthorhombic *Cmcm* structure to another orthorhombic *Pmnm* structure (HP1 phase). Our Raman experiments reveal another phase transition at $P \sim 10$ GPa. While we do not find a transition at pressure (HP2) phase (observed at $P \sim 10$ GPa) our calculations suggest a reduction in band gap of the semiconducting HP1 structure with pressure, and a possibility of pressure-induced insulator to metal transition within the HP1 phase. We hope our study will provoke further experimental and theoretical studies to understand the second phase transition better.

ACKNOWLEDGMENTS

A.K.S. acknowledges National Science Chair Professorship for financial support. S.P acknowledges DST for Inspire fellowship. A.S. is thankful to JNCASR for a research fellowship. U.V.W. acknowledges support through a J. C. Bose National fellowship of SERB-DST, Government of India. L.H. acknowledges financial support from DST-India (DST/WOS-A/PM-83/2021 (G)) and National Mission on Interdisciplinary Cyber-Physical Systems (NM-ICPS) of the Department of Science and Technology, Government of India through the I-HUB Quantum Technology Foundation, Pune, India, and IISER Pune for providing crystal growth and characterization facilities.

[1] R. S. Knox, Theory of excitons, in *Solid State Physics* (Academic Press, New York, 1963).

[2] B. I. Halperin and T. M. Rice, Possible anomalies at a semimetal-semiconductor transition, Rev. Mod. Phys. **40**, 755 (1968).

[3] D. Jérome, T. M. Rice, and W. Kohn, Excitonic insulator, Phys. Rev. **158**, 462 (1967).

[4] J. A. Wilson, Concerning the semimetallic characters of TiS_2 and $TiSe_2$, Solid State Commun. **22**, 551 (1977).

[5] H. Cercellier, C. Monney, F. Clerc, C. Battaglia, L. Despont, M. G. Garnier, H. Beck, P. Aebi, L. Patthey, H. Berger, and L. Forró, Evidence for an excitonic insulator phase in $1T$-$TiSe_2$, Phys. Rev. Lett. **99**, 146403 (2007).

[6] B. Bucher, T. Park, J. D. Thompson, and P. Wachter, Thermodynamical signatures of an excitonic insulator, arXiv:0802.3354.

[7] P. Wachter, Exciton condensation in an intermediate valence compound: $TmSe_{0.45}Te_{0.55}$, Solid State Commun. **118**, 645 (2001).

[8] P. Wachter, The discovery of excitonium, J. Alloys Compd. **225**, 133 (1995).

[9] Y. F. Lu, H. Kono, T. I. Larkin, A. W. Rost, T. Takayama, A. V. Boris, B. Keimer, and H. Takagi, Zero-gap semiconductor to excitonic insulator transition in Ta_2NiSe_5, Nat. Commun. **8**, 14408 (2017).

[10] D. Werdehausen, T. Takayama, M. Höppner, G. Albrecht, A. W. Rost, Y. Lu, D. Manske, H. Takagi, and S. Kaiser, Coherent order parameter oscillations in the ground state of the excitonic insulator Ta_2NiSe_5, Sci. Adv. **4**, eaap8652 (2018).

[11] A. Nakano, K. Sugawara, S. Tamura, N. Katayama, K. Matsubayashi, T. Okada, Y. Uwatoko, K. Munakata, A. Nakao, H. Sagayama, R. Kumai, K. Sugimoto, N. Maejima, A. Machida, T. Watanuki, and H. Sawa, Pressure-induced coherent sliding-layer transition in the excitonic insulator Ta_2NiSe_5, IUCrJ **5**, 158 (2018).

[12] Y. Wakisaka, T. Sudayama, K. Takubo, T. Mizokawa, M. Arita, H. Namatame, M. Taniguchi, N. Katayama, M. Nohara, and H. Takagi, Excitonic insulator state in Ta_2NiSe_5 probed by photoemission spectroscopy, Phys. Rev. Lett. **103**, 026402 (2009).

[13] S. A. Sunshine and J. A. Ibers, Structure and physical properties of the new layered ternary chalcogenides tantalum nickel sulfide (Ta_2NiS_5) and tantalum nickel selenide (Ta_2NiSe_5), Inorg. Chem. **24**, 3611 (1985).

[14] T. I. Larkin, A. N. Yaresko, D. Pröpper, K. A. Kikoin, Y. F. Lu, T. Takayama, Y.-L. Mathis, A. W. Rost, H. Takagi, B. Keimer, and A. V. Boris, Giant exciton fano resonance in quasi-one-dimensional Ta_2NiSe_5, Phys. Rev. B **95**, 195144 (2017).

[15] M. Ye, P. A. Volkov, H. Lohani, I. Feldman, M. Kim, A. Kanigel, and G. Blumberg, Lattice dynamics of the excitonic insulator $Ta_2Ni(Se_{1-x}S_x)_5$, Phys. Rev. B **104**, 045102 (2021).

[16] L. Li, P. Gong, W. Wang, B. Deng, L. Pi, J. Yu, X. Zhou, X. Shi, H. Li, and T. Zhai, Strong In-plane anisotropies of optical and electrical response in layered dimetal chalcogenide, ACS Nano **11**, 10264 (2017).

[17] F. J. Di Salvo, C. H. Chen, R. M. Fleming, J. V. Waszczak, R. G. Dunn, S. A. Sunshine, and J. A. Ibers, Physical and structural properties of the new layered compounds Ta_2NiS_5 and Ta_2NiSe_5, J. Less-Common Met. **116**, 51 (1986).

[18] K. Okazaki, Y. Ogawa, T. Suzuki, T. Yamamoto, T. Someya, S. Michimae, M. Watanabe, Y. Lu, M. Nohara, H. Takagi, N. Katayama, H. Sawa, M. Fujisawa, T. Kanai, N. Ishii, J. Itatani, T. Mizokawa, and S. Shin, Photo-induced semimetallic states realised in electronhole coupled insulators, Nat. Commun. **9**, 4322 (2018).

[19] S. Pal, S. Grover, L. Harnagea, P. Telang, A. Singh, D. V. S. Muthu, U. V. Waghmare, and A. K. Sood, Destabilizing excitonic insulator phase by pressure tuning of exciton-phonon coupling, Phys. Rev. Res. **2**, 043182 (2020).

[20] N. Pistawala, D. Rout, K. Saurabh, R. Bag, K. Karmakar, L. Harnagea, and S. Singh, Crystal growth of quantum materials: A review of selective materials and techniques, Bull. Mater. Sci. **45**, 10 (2022).

[21] H. K. Mao, J. Xu, and P. M. Bell, Calibration of the ruby pressure gauge to 800 kbar under quasi-hydrostatic conditions, J. Geophys. Res. Solid Earth **91**, 4673 (1986).

[22] QUANTUM-ESPRESSO is a community project for high-quality quantum-simulation software, based on density-functional theory, and coordinated by P. Giannozzi. See http://www.quantum-espresso.org and http://www.pwscf.org.

[23] A. Dal Corso, Pseudopotentials periodic table: From H to Pu, Comput. Mater. Sci. **95**, 337 (2014).

[24] J. P. Perdew, K. Burke, and M. Ernzerhof, Generalized gradient approximation made simple, Phys. Rev. Lett. **77**, 3865 (1996).

[25] J. Klimeš, D. R. Bowler, and A. Michaelides, Chemical accuracy for the van der Waals density functional, J. Phys.: Condens. Matter **22**, 022201 (2010).

[26] T. Thonhauser, S. Zuluaga, C. A. Arter, K. Berland, E. Schröder, and P. Hyldgaard, Spin signature of nonlocal correlation binding in metal-organic frameworks, Phys. Rev. Lett. **115**, 136402 (2015).

[27] T. Thonhauser, V. R. Cooper, S. Li, A. Puzder, P. Hyldgaard, and D. C. Langreth, Van der Waals density functional: Self-consistent potential and the nature of the van der Waals bond, Phys. Rev. B **76**, 125112 (2007).

[28] K. Berland, V. R. Cooper, K. Lee, E. Schröder, T. Thonhauser, P. Hyldgaard, and B. I Lundqvist, van der Waals forces in density functional theory: A review of the vdW-DF method, Rep. Prog. Phys. **78**, 066501 (2015).

[29] D. C. Langreth, B. I Lundqvist, S. D Chakarova-Käck, V. R. Cooper, M. Dion, P. Hyldgaard, A. Kelkkanen, J. Kleis, L. Kong, S. Li, P. G. Moses, E. Murray, A. Puzder, H. Rydberg, E. Schröder, and T. Thonhauser, A density functional for sparse matter, J. Phys.: Condens. Matter **21**, 084203 (2009).

[30] R. Sabatini, E. Küçükbenli, B. Kolb, T. Thonhauser, and S. D. Gironcoli, Structural evolution of amino acid crystals under stress from a non-empirical density functional, J. Phys.: Condens. Matter **24**, 424209 (2012).

[31] V. I. Anisimov, J. Zaanen, and O. K. Andersen, Band theory and Mott insulators: Hubbard U instead of stoner I, Phys. Rev. B **44**, 943 (1991).

[32] M. Cococcioni and S. de Gironcoli, Linear response approach to the calculation of the effective interaction parameters in the LDA+U method, Phys. Rev. B **71**, 035105 (2005).

[33] See Supplemental Material at http://link.aps.org/supplemental/10.1103/PhysRevB.109.155202 for additional supporting experimental and theoretical results. The Supplemental Material also contains Ref. [34].

[34] M. A. Ruiz Preciado, A. Kassiba, A. Morales-Acevedoc, and M. Makowska-Janusik, Vibrational and electronic peculiarities of $NiTiO_3$ nanostructures inferred from first principle calculations, RSC Adv. **5**, 17396 (2015).

[35] A. Togo and I. Tanaka, First principles phonon calculations in materials science, Scr. Mater. **108**, 1 (2015).

[36] A. Togo, K. Shinohara, and I. Tanaka, Spglib: A software library for crystal symmetry search, arXiv:1808.01590.

[37] K. Mu, H. Chen, Y. Li, Y. Zhang, P. Wang, B. Zhang, Y. Liu, G. Zhang, L. Song, and Z. Sun, Electronic structures of layered Ta_2NiS_5 single crystals revealed by high-resolution angle-resolved photoemission spectroscopy, J. Mater. Chem. C **6**, 3976 (2018).

[38] A. Subedi, Orthorhombic-to-monoclinic transition in Ta_2NiSe_5 due to a zone-center optical phonon instability, Phys. Rev. Mater. **4**, 083601 (2020).